Challenges and Opportunities of Thermography in Metallurgy

Alexander Specht and Bernd Friedrich

Abstract

High process control and product quality standards in industry and scientific research demand exact temperature determination for metallurgical systems. In many cases, reliable information can be obtained via thermocouple measurements. Still, this option is unfeasible for technologically advanced processes such as consumable vacuum arc remelting due to technical reasons, for example, high temperatures, aggressive melts, or demand for melt cleanliness. Those circumstances necessitate contactless infrared measurement to ensure accurate and non-invasive results. Determining thermal emissivity, the harsh environment, and the dynamic of liquid surfaces in the process are challenging conditions for infrared thermography in metallurgy. However, in return, it allows measuring online with high resolution in time and space at the surface of a metallurgical process, quantifying the amount of superheating or temperature development over time and to detect phases with different thermal emissivity, like slag on metallic phases. This information can be used to increase simulation accuracy, microstructure prediction, as well as process control and comprehension. The study introduces IR-thermography for metallurgical applications with practical examples and demonstrates its successful implementation in a titanium alloy consumable electrode vacuum arc remelting.

Keywords

Infrared thermography · Process control · Pyrometallurgy · Recycling · Remelting · Titanium · Vacuum arc remelting

1 Introduction

Infrared thermography describes colour or contrast imaging of surficial temperature distribution, obtained from measured thermal radiation data. The principles of infrared (IR) radiation and the technological advancements necessary to detect it have been investigated in the 1800s. William Hershel observed how light refracted through a prism heated its target depending on its colour, and deduced that thermal radiation outside the visible spectrum must be responsible [1]. This groundwork was then refined by the contributions of Gustav Kirchhoff [2], Joseph Stefan [3], and Ludwig Boltzmann [4], whose names can today still be found in the Stefan-Boltzmann's law.

The thermopile introduced by Nobili Leopoldo in 1830 [5] laid the foundation for modern day bolometers, but it wasn't until WWI that IR technology became interesting for military applications and was therefore developed to its modern performance in secret [6]. Up to this day, defence and surveillance are important application areas for IR technologies to uncover otherwise invisible threads. With the end of the "Cold War", IR technology became available to the public, opening up opportunities for new use cases [6]. Today, thermal imaging can be found in agriculture [7], medicine [8, 9], biological studies [10], civil engineering [11, 12], industry [13, 14], material science [15], and many more.

A. Specht (✉) · B. Friedrich
Institute and Chair for Process Metallurgy and Metal Recycling at RWTH Aachen University, Aachen, Germany
e-mail: ASpecht@ime-aachen.de

Proceedings of the 62nd Conference of Metallurgists, COM 2023, https://doi.org/10.1007/978-3-031-38141-6_33

In metallurgy, most attention is brought to subjects of ladle and/or furnace insulation for increased thermal efficiency, refractory lining condition determination [16–18] as well as slag detection systems [19, 20]. However, only little to no information concerning in-process melt observation and temperature surveillance can be found in literature. This is due to the difficult nature of IR thermography on liquids and reflective surfaces, such as unoxidized metals, the determination of accurate estimates for emissivity, and the compensation for changing transmittance in the system. In this study, four different metallurgical setups with their special requirements for accurate temperature determination as well as further evaluable observations are presented. For consumable vacuum arc remelting (VAR), a specialized evaluation method is presented that delivers robust and representative data evaluation, when interpreting IR thermography for VAR.

2 Background for IR Thermography in Pyrometallurgy

Other than contact temperature measurements, such as thermocouples or resistance thermometers, which rely on a heat induced voltage change in the sensor material, IR thermography is dependent on the measured materials emittance and the transmittance, of the medium in between the measured spot and the detector. Values for emittance can be found in literature for some materials, allowing a rough estimate, but for exact measurements even small differences in surface condition, such as state of oxidization or surface roughness can have major influence on emissivity [14].

Spectral Range IR radiation is part of the electromagnetic spectrum and defined as the spectrum between 0.75 and 1000 µm, sitting in between visible light and radio waves. This spectrum is then divided into subspaces, for which different technical literature has found varying limits. In IR thermography 3–5.5 µm (short wave IR, SWIR) and 7–14 µm (long wave IR, LWIR) are established boundaries, since the commonly used InSb and CdTeHg IR detectors cover those wave lengths [14, 21]. The shorter wave length section between 0.7 and 1.4 µm is referred to as near IR (NIR), which is most interesting for pyrometallurgical processes, because radiant exitance curve according to Plank's formula reach their maximum in said interval. The stronger signal allows for better separation of data from noise, delivering more accurate results of NIR thermal imagers at high temperatures [21–23].

Determination Emissivity The deviation from the ideal curve of a blackbody to the observed graybody curve is considered by the emissivity, which ranges between 0 and 1. This value is temperature, material, and observation angle dependent, making calibration of the imager necessary according to the observed system [21, 24]. Common methods for emissivity determination include painting parts of the observed subject or attaching stickers with a known emissivity and compare it to uncovered surface [21]. Those methods have low limited maximum temperature which make them unsuitable for pyrometallurgical applications. Possible options for emissivity determination are matching the IR values with a thermocouple measurement or the observation of phase transformations and a comparison with calculated/literature values.

Transmittance and Optical Disturbances The second important property in an IR system is transmittance of the IR radiation in the media, that lie between the source and the detector [14, 21]. For metallurgical setups, medias appear in manifold form, for example, standard atmosphere, dust, smoke, combustion gases, inert gas or vacuum. Furthermore, glass at viewports with and without coatings of dust and condensed vapours will influence transmittance, making an accurate assessment additionally challenging. Transmittance of glasses can be determined with a setup, where the temperature of a known substance is measured with and without the glass to determine its transmittance, which works well for a before and after calibration. A continuous calibration during the trial/process to detect a shift in transmission is only possible with a known temperature reference in the field of view or other technical solutions such as an online spectrometer. An easier solution is to shield glasses with an argon veil at the viewport to prevent contamination. Further interferences can be caused by stray heat sources, which reflect on measured surfaces. To avoid errors through these influences, users have to carefully design their setup and take possible disturbances into account, when evaluating the data, especially in complex setups such as smelting trials to generate reliable and comprehensible measurements.

3 Examples for IR Thermography in Metallurgy

In this chapter, four experimental setups are shown, which have been observed via IR imaging. All measurements were performed with a "PYROVIEW 768N / 50 Hz compact+" IR thermal imager by "DIAS Infrared Systems GmbH" (Dresden Germany) via their software "PYROSOFT Professional" Version 5.5.4.3 on a Win10 PC [25]. An excerpt from the technical information is noted in Table 1.

3.1 Al-Skimming

Experiment In this first example, commercial pure aluminium (>99.99 wt.% Al) was molten in a clay-graphite crucible in a 3 kHz induction furnace under atmospheric conditions. The Al-feedstock was molten and the melt was superheated to approximately 800 °C to allow for an oxide layer formation. Then, the induction coil is powered off to achieve an even melt surface. The oxide layer was skimmed, using a Boron-Nitride (BN) coated spoon. Temperatures range in between 750 °C and 800 °C during skimming, so a temperature measurement is not possible with the imager calibration, but using a high emissivity and transmittance setting of 0.1 each, did allow to create a visual image anyways. The imager was mounted at a distance of 120 cm over the melt surface at an angle of 80° relative to the melt surface. Resulting images are presented in Fig. 1.

Table 1 Technical specifications "PYROVIEW 768N / 50 Hz compact+" IR thermal imager [25]

Parameter	Value
Spectral range	0.8–1.1 µm
Sensor	Uncooled Si-CMOS-Array
Resolution	768 × 576 px
Max. measurement frequency	50 Hz
Measurement temperature range	800–2500 °C
Measurement uncertainty	2% of measured value in °C
FOV lens	39° × 30°

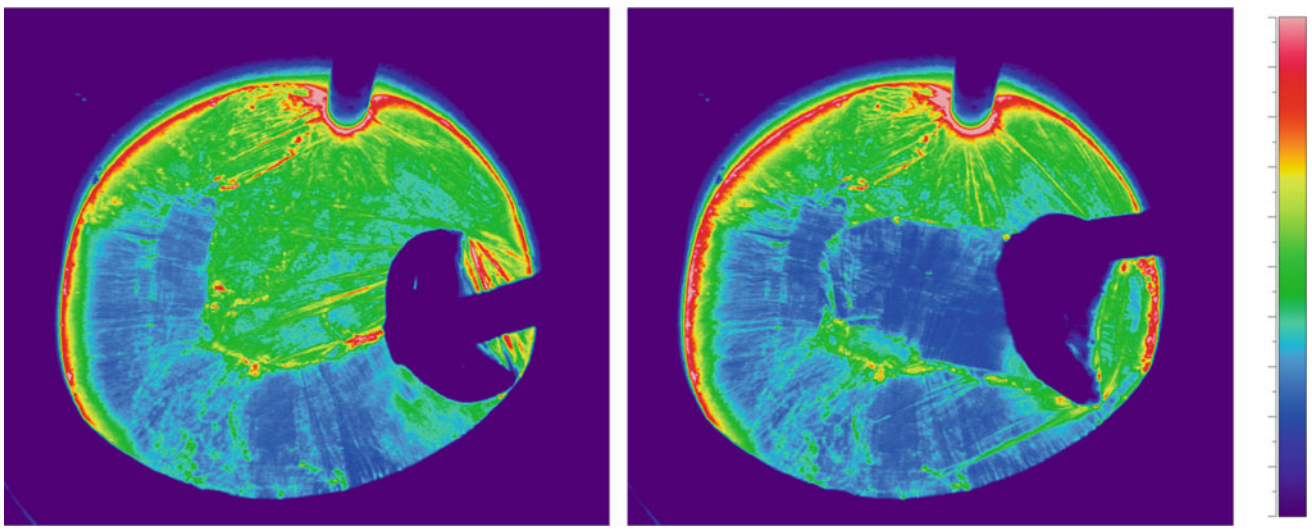

Fig. 1 Melt surface of Al-melt after first (left) and second skimming movement (right) with temperature scale bar at imager settings of ε: 0.1 and τ: 0.1

Result The two images show the melt surface with the used spoon after two consecutive skimming operations. The first one was made counter-clockwise at the lower crucible side and the second one from left to right in the middle. The skimming reveals a blue coloured surface, while at the tip of the spoon red waves form, creating the impression of a skin that is being scraped of the surface. At the edges of the skimmed surface red and yellow clumps form the boundary between skimmed and unskimmed surface. At the contact surface between melt and crucible as well as between melt and thermocouple protection tube, a red ring is visible for the area where the meniscus curvature is to be expected due to wettability reasons.

Discussion Assuming a homogenous temperature at the surface, the colours representing the temperature scale should be interpreted as a rudimentary scale for oxide layer thicknesses, where blue is thin and red is thick. This is due to the fact, that the detector does not differentiate between thermal emissivities. In consequence areas of higher emissivity seem "hotter" than those with lower emissivity at the same temperature. This explains the colour shift from green to blue while skimming and the red and yellow areas at the front of the spoon and the sides of the skimmed area, since the newly revealed surface is covered by only an instantly formed, very thin Al-oxide layer, while on the other aforementioned parts thicker oxides were developed during heating and melt holding period. The edge areas touching the crucible and thermocouple protection tube also seem hotter but, in these areas, it is not the change in emissivity but the reflection of the IR radiation from the refractory materials is mixed with the thermal emissivity of the Al.

Conclusions Even though a temperature reading isn't possible in this setup, valuable information can be obtained from the images. Oxide skin on the melt surface, which is sometimes hard to be identified or even invisible to the eye, is revealed. Through thermal imaging, information with regards to position of residual oxide and thickness evolution were made available. This could be helpful in every metallurgical situation, where skimming or manual de-slagging is needed to ensure product quality and cost efficiency. With adequate skimming, metal losses to the dross can be minimized and non-metallic inclusions such as oxide in the melt can be largely reduced.

3.2 Aluminothermic Reduction

Experiment The second trial observed the aluminothermic reduction (ATR) of metal oxides to create an equimolar AlCrMoTiV high entropy alloy. Oxides of Ti, Cr, Mo, Nb, V, and Ca were mixed with $KClO_4$ and Al to create approximately 15 kg of autothermal reaction mixture. After weighing and thorough mixing in a tumble mixer, the material was placed in a reaction vessel made from cast alumina refractory lining. The reaction was started by electric ignition after which it is self-sustaining. Smoke generated by reaction was captured in a flue gas system.
The imager was mounted on an Al-beam construction, at 110 cm distance and an angle of 70° relative to the melt surface. For protection, 1.5 mm steel plating with a quartz glass viewport was used to avoid damage by ejected material from the reaction vessel. Transmissivity of the glass is known to be 0.93 and therefore set accordingly. In addition, thermocouple measurement inside the reaction material was performed with type C thermocouples in graphite protective tubes that were placed inside the alumina refractory lining. Emissivity for the liquid phase is determined to be 0.90 by matching the thermocouple measurement to IR-measurements.

Result Thermal imaging in ATR is confronted with the production of particle rich off gas caused by the reaction. This is visible on the left-hand side in Fig. 2, where thick fume is blocking nearly all IR-radiation, making temperature measurements impossible in this setup. When the reaction decreases around 1:15 min:ss, smoke generated by the reaction does not disturb vision anymore and the bath movement induced by free convection becomes visible. At 1:30 min:ss, first temperature measurements become possible, where red areas range between 1750 °C and 1800 °C and the remaining liquid represented in orange, shows temperatures between 1610 °C and 1630 °C. Also, a solid area in yellow to green colour forms and is measured to be around 1430–1500 °C.

Discussion After the decreased smoke development, bath movements became visible, which are caused by streams of hot slag rising with gas bubbles from the ongoing reaction of unreacted material. The detected temperature differences of 120–190 °C illustrate how fast the heat from reaction is lost to the surroundings via radiation and conductive mechanisms. The deduction of these mechanisms is only possible due to the high responsiveness of the imager. A comparable study with thermocouples would be impossible due to their lower responsiveness. The growth of solidifying material can easily be

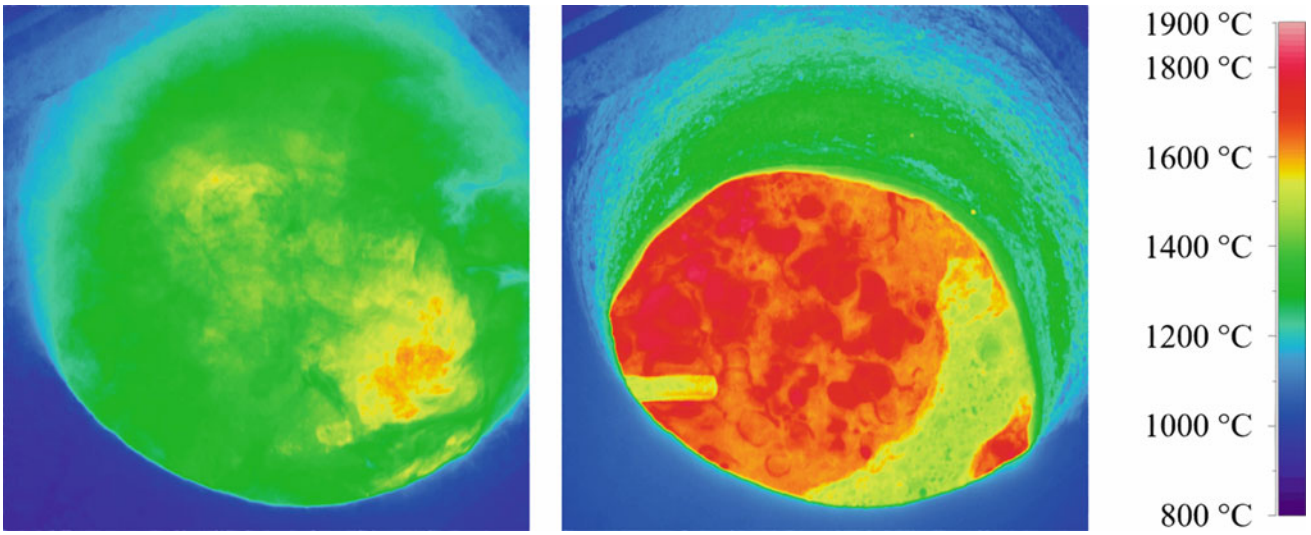

Fig. 2 Thermal image of ATR in reaction vessel, 1 min after ignition (left) and 2 min after ignition with visible thermocouple (right) with temperature scale bar at imager settings of ε: 0.9 and τ: 0.93

detected by the bright green and yellow color. This is caused in part by the temperature of the material, but also the change in emissivity at the phase transition, which allows good traceability for the solidification front. Temperature measurements of the solid slag have to be done on a separate setting to ensure accuracy, since the imager is calibrated for the liquid phase.

Conclusions Smoke blocking the NIR spectrum as well as visible light is an issue in thermography, but can be overcome with a longwave IR imager. Long wave IR offers low measurement accuracy in high temperature conditions, but offer a clear view through smoke to observe the process in all stages [17, 23]. In such cases, users have to decide on the information that brings greater value for their specific process, or install systems with different spectral ranges. For the second part of the trial, IR imaging delivers insight on the inhomogeneous heat distribution caused by the autothermal reaction close to the bottom versus the cooler surface area. This information is useful in process simulation or creation of a heat balance.

3.3 Non-consumable Vacuum Arc Melting

Experiment In this setup, 114 g of TiAl alloy GE48-2-2 with a calculated liquidus temperature around 1510 °C [26] was remolten in an "AM500"non-consumablevacuum arc melter (Edmund Bühler GmbH; Bodelshausen, Germany) from pre-molten and crushed material as shown in Fig. 3. The material was put into the water-cooled Cu-mold, a vacuum of $<3*10^{-2}$ mbar was drawn and the furnace was flushed with Ar (99.998% Ar) to a pressure of approx. 700 mbar. The arc was ignited on the side of the mold after which the material was molten in 01:42 mm:ss with circular motions of the W-electrode to decrease local overheating. The melting and subsequent cooling was captured at 50 Hz via thermal imager. The imager is mounted at an angle of 50° relative to the pool surface at a distance of 40 mm, looking through borosilicate glass. Before and after the smelting, the glass transmittance was determined to be 0.77 via measurements of a graphite block at 1000 °C in a resistance heated furnace. Thermal emissivity is determined to be 0.61 by matching the liquidus temperature of 1510 °C with the confirmation of visually detected solidification.

Result Temperature measurement during the melting time is corrupted due to the strong thermal emission of the arc and the reflective metal surface. Temperatures after arc extinguishing are evaluated over time at the values of interest (VOI) 001-005 and displayed as a graph in Fig. 4. At 0.06 s after arc extinguishing, temperatures of approx. 1540 °C are measured across the pool surface, which represents a superheating of 30 °C. During the first second, temperature decreases to 1510 °C and in the time of 1.0–4.0 s after arc extinguishing a plateau form at 1510 °C for VOI 003-005, after which temperature drops in all VOIs. The calculated cooling rates show great similarity in curve path and differ only in some details on length and pronunciation of certain transitions. Similarities for all VOIs are the formation of a peak at the corresponding temperatures of 1390 ± 10 °C and the two plateaus in the rate at 1300 ± 10 °C and 1210 ± 10 °C.

Fig. 3 Arc melter setup at Access technologies GmbH with thermal imager (left); Cu-mold with crushed material before trial (top right); Cu-mold with remolten material after trial (bottom right)

Discussion The solidification and solid state transformation for the system is modelled in FactSage™ [26]. The system shows the following phase transitions during solidification according to Eq. 1.

$$\text{liquid} \xrightarrow{1510\,^\circ\text{C}} \text{liquid} + \beta Ti \xrightarrow{1396\,^\circ\text{C}} \alpha Ti + \beta Ti + \gamma\text{TiAl} \xrightarrow{1290\,^\circ\text{C}} \beta Ti + \gamma\text{TiAl} \xrightarrow{1230\,^\circ\text{C}} \gamma\text{TiAl} \quad (1)$$

The liquidus transitions is easy to spot even in the temperature graph as the plateau at 1510 °C. The following transitions are visible only in the cooling rate graph. The peak in the cooling rate at 1390 °C matches the solidus temperature which is to be at 1396 °C. The plateaus at 1300 and 1200 °C are in good agreement with the first and second solid-solid transformation. There are deviations of the measured values from the calculated ones; however, the calculation is done for equilibrium conditions, which the rapid cooling in the trial does not represent. The above-shown values therefore only represent rough estimates for transition temperatures in the observed system. Additionally, accuracy of the measured values has to be viewed critically, since the imager specific measurement uncertainty of 2% of measured temperature in °C is rather large at ±30 °C, if absolute values are considered. On the other hand, comparable thermocouples usually show similar values for uncertainty at around 1.5% of measured temperature in °C depending on thermocouple type [27]. Uncertainty can therefore be considered as less of an IR-thermography, but general high temperature measurement challenge.

Conclusions IR thermography has shown capable to determine the cooling rate of solidifying metals and even phase transformations in this trial. Small shifts in cooling rate are detectable and allow for conclusions regarding liquid-solid as well as solid-solid transformations, similar to differential thermal analysis. The fact that no physical contact is needed ensures low latency and zero influence on the measurement by the equipment. Also, retroactive location choice is possible, allowing to

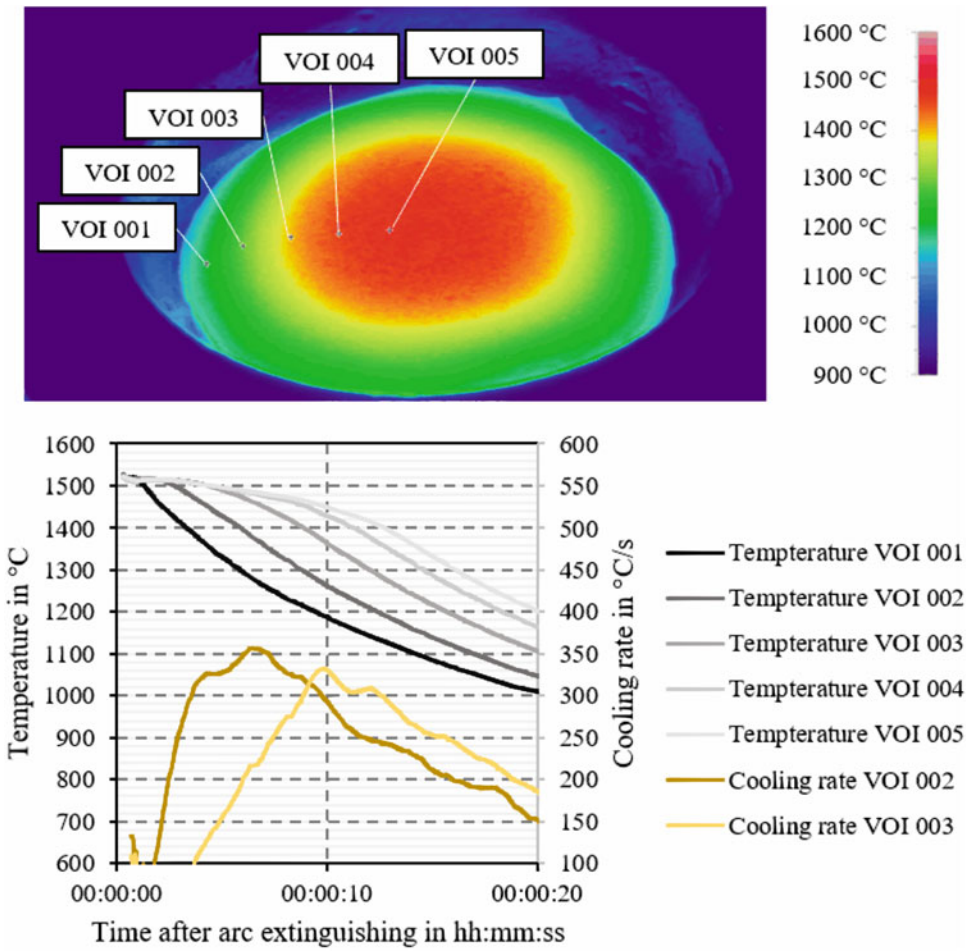

Fig. 4 Thermal image of GE48-2-2 metal button 10 s after arc extinguishing in arc melter with temperature scale bar at ε: 0.61 and τ: 0.77 with the location of virtual thermocouples (top); temperature over time at the positions of the virtual thermocouples, without any smoothening on the primary axis and cooling rates for VOI 002 & VOI003 on secondary axis (bottom)

investigate unforeseen events in previously unobserved areas. Measurement accuracy is a challenge, but can be managed by proper calibration and is comparable to thermocouple measurements in that temperature range, which are state of the art in metallurgy.

3.4 Consumable Electrode Vacuum Arc Remelting

Vacuum arc remelting is a process to optimize metal ingot quality with regard to chemical and microstructural homogeneity. In VAR, the electrode, made from compacted metallic material or cast ingot, is continuously remolten under vacuum atmosphere. The process requires a good knowledge of the thermal system and has therefore been subject to multiple computational studies. The developed models mostly rely on a microstructural analysis after the remelt, giving information on the solidification behaviour to validate the simulation. A conventional temperature measurement via contact measurement is unsuitable for temperature detection in VAR owing to the extreme environment inside the furnace such as high currents and temperatures. In this exemplary remelt, thermal imaging is presented as a tool to gather additional information on the remelting process for computational studies and to increase understanding in this complex process.

A second motivation for this investigation is the future endeavour at IME – RWTH to test online feeding of powder material of the same species or alloying material into the pool during VAR, to influence its temperature and therefore solidification behaviour. Detection of direct temperature feedback in the process in addition to metallographic examination of the final ingot is key information to understand the underlying principles. This is why a robust evaluation method for IR

images from VAR process was developed, allowing to link temperature changes to process parameters such as gap distance or current input.

Experiment In the case study, the remelt of a solid GE48-2-2 ($Ti_{48}Al_{48}Nb_2Cr_2$) alloy electrode with a diameter of 160 mm into a crucible diameter of 200 mm in a consumable electrode VAR, "VAR L 200" from ALD Vacuum Technologies GmbH (Hanau Germany) was observed via thermal imaging and optical camera. The imager was mounted outside the furnace, parallel to the electrode rod, looking through two panes of glass, one tempered glass and one protective quartz glass and through the ring gap between electrode and crucible, onto the pool surface at an angle of 90°. The transmittance of the two panes was determined to be 0.67 via reference measurement of graphite in a resistance heated furnace. Emissivity was determined to be 0.38 via the solidification observation and matching to the calculated liquidus temperature of 1510 °C. The distance between the camera and pool surface decreases over time due to the rising ingot, subsequently focus was adjusted manually over time. After assembly, the furnace was evacuated to $<8 \times 10^{-5}$ mbar, flushed with Ar (99.998% Ar) to a pressure 600 mbar and evacuated again to working pressure of $<3 \times 10^{-2}$ mbar. During the trial, the vacuum pumps were in continuous operation. The process parameters gap length and arc power were controlled manually and varied throughout the trial to evaluate their impact on pool temperature and to test IR thermal imaging capabilities to detect temperature differences, caused by these changes. Used process parameters of the three stages in the trial are shown in Table 2. First arc power was varied between 2.1 and 2.5 kA, followed by a steady state phase at 2.4 kA, at gap distances of around 1.5 cm. In the third part, arc power was kept constant, but gap distance was continuously increased to 2.5 cm, while the end of the electrode was reached.

Result The thermal images are evaluated at the eight positions, marked in Fig. 5 which show a broad distribution between 1482 °C and 1978 °C in the melt phase. Lower temperatures are located in the yellow spots in the image, which move over the pool surface with the wave motions over the "hot" background marked red in image. If compared to the optical camera feed it can be seen that most of the pool surface reflects the electrode underside and its radiated heat similar to the red areas in the IR

Table 2 Process parameters for trial stages a, b, and c

Trial stage	Time after ignition, min	Avg. current, kA	Avg. Voltage, V	Avg. gap distance, cm
a	16–22	2.1, 2.4, 2.5	23	1.5
b	24–30	2.4	23	1.5
c	32–38	2.4	23	1.5–2.5

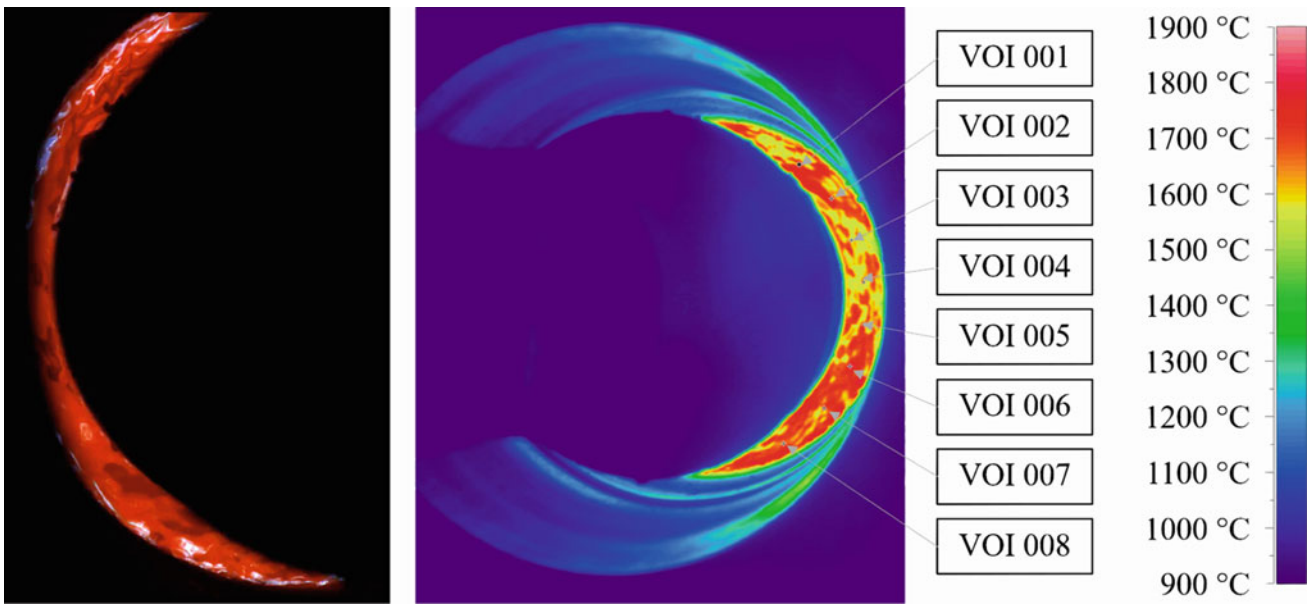

Fig. 5 Images during remelting at 29 min after arc ignition from camera feed (left) and thermal imager (right) with marked positions for virtual thermocouples with temperature scale bar at ε: 0.38 and τ: 0.67

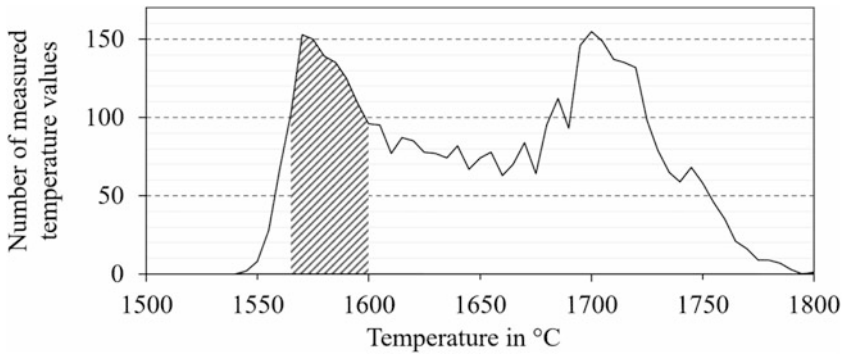

Fig. 6 Temperature histogram example for 24:00-24:10 min:ss between 1500 °C and 1800 °C with marked area for temperature evaluation

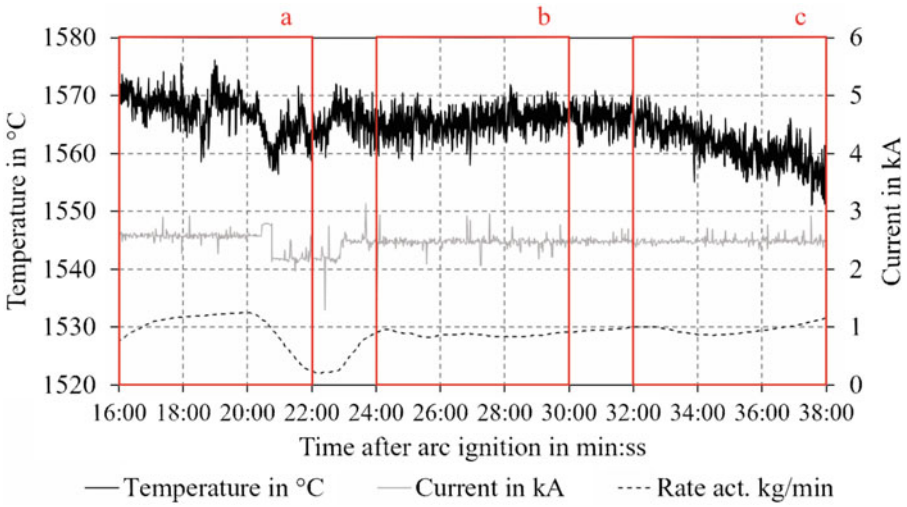

Fig. 7 Pool temperature and current over time in the three trial stages

image. Only in the valleys between waves, darker spots are observed. Contrary to what the image suggests, the reflective metal surface makes it difficult to observe through the camera, as it is often overexposed by the bright light from the arcs. The IR images showed a better dynamic range than the camera feed, allowing for a better observation of the wave motions.

For reliable temperature measurement, the temperature data must therefore be filtered to eliminate measurements superimposed by reflections. Truncating data at fixed min- and max-values causes a deviation from the true temperature value. Consequently, dynamic limits are employed by calculating a histogram for a time period of 10 seconds as shown in Fig. 6, where the two overlapping signals can be made out. Then the marked peak on the left represents the pool temperature, while the right peak at approx. 1710 °C represents the overlapped signal from the pool emission together with electrode underside reflection.

The limits from the histogram are used to trim the temperature data for the correlated timeframe and the average value is calculated from the remaining values. The steps are then repeated after moving the observed frame one second further, thus creating a moving average. The resulting temperature graph, recorded arc current and gap melt rate are shown in Fig. 7 for the three stages in the trial. Three different temperature responses were observed. For section (a), temperature was mostly stable at approx. 1570 °C, until current was lowered at 20:30 min:ss, where melt rate and temperature dropped simultaneously. In section (b) temperature was constant over the observed time at constant power input and melt rate. Section (c) shows a linear decline in temperature at constant power input and slight increase in melt rate.Other changes not shown in the image are the growing gap length and a measured rise in pressure from 2×10^{-2} mbar to1×10^{-1} mbar without any changes to the vacuum system.

Discussion Thermal imaging needs special data treatment for its application in VAR, but shows good responsiveness of temperature readings to changes in melt rate and gap length. The temperature decrease in stage (c) could have multiple reasons. Its link to the slight rise in melt rate is unlikely, since in stage (a) the decrease in temperature is accompanied by a decrease in temperature. Considering the rise in pressure towards the end of the process and the fact that the electrode was

nearly consumed in the end, it is to be suspected that due to overheating of the residual electrode material, a higher amount of metal vapour than in steady state was produced. This has a direct influence on the measurement as well as on the arc mode. The higher metal vapour pressure in the gap represents favourable conditions for a glow discharge, which has a lower heat output at comparable power input, thus explaining the temperature decrease. Another consequence of increased metal vapor in the furnace could be the build-up of thin metal coatings on the glass, decreasing transmittance. Although no change in transmittance was detected in a second check of the glass after the trial, this possibility cannot be ruled out, since a minor change in transmittance can cause a great change in temperature value at the observed temperatures.

Conclusions Measurement for pool temperature in VAR has been successfully implemented via dynamic evaluation limits and a moving average. The deduced temperatures can be linked to the corresponding process parameters arc power, melt rate, and gap length. In addition to this, thermal images allow for great observability of the pool surface motions without disturbance by the arcs bright light.

The decreased temperature in stage (c) cannot be linked to a definite cause without further testing, but it is strongly suspected that either a change in arc mode or vapour coating of the glass is responsible. Concluding IR thermography is considered to be suitable to detect temperature shifts and will therefore be used in trial with online feeding to evaluate its impact on temperature.

4 Summary and Outlook

Thermal imaging produced valid temperature measurements for metallurgical applications and delivered additional data compared to conventional methods of temperature measurement regarding temperature distribution and detection of otherwise invisible differences in phases. Accurate temperature measurements remain challenging for complex systems, such as metallurgical setups and in some cases may even be unfeasible due to optical disturbances. These are observed at the presence of extreme radiation sources like open arcs, reflective, and uneven liquid metal surfaces, contaminated glass of viewports or smoke in the atmosphere. However, for most cases, a carful designed trial setup and data interpretation allow to extract temperature readings as well as detailed images of melt surface with high contrast between existing different phases. As a result, it has been demonstrated that temperature measurements in ATR, vacuum arc melting, and VAR are possible. The presented filter for pool temperature data in VAR process delivers comprehensible results and is expected to fit the needs of the planned trials of VAR with online feeding.

Other than this, IR imaging shows qualities suitable not only for temperature detection in metallurgical research but also for multiple scenarios such as skimming control and automatization, worker and student education or phase transformation observation. In this study, only one imager system in NIR spectrum was employed, leaving room for additional testing with IR thermography in other parts of the thermal radiation spectrum with their respective challenges and opportunities. Further interesting additions would be the implementation of IR spectrometers and quotient−/pyrometers to increase comprehension and to facilitate detection of shifts in transmittance and emittance.

Acknowledgements This research was funded by the German Federal Ministry of Education and Research, grant number: 03HY111E
The author thanks Pierre Chapelle and Julien Jourdan – Institut Jean-Lamour, Université de Lorraine – for the exchange on technical issues.
The author further acknowledges the experimental work of Carolin Maier – IME, RWTH Aachen University – (ATR trial), Cong Li – IME, RWTH Aachen University – (Al-skimming trial), Sergej Gein – Access e.V. – (non-consumable electrode electric arc melting trial). Thank you all for letting me film your trials!

References

1. Hershel W (1800) XIII. Investigation of the powers of the prismatic colours to heat and illuminate objects; with remarks, that prove the different refrangibility of radiant heat. To which is added, an inquiry into the method of viewing the sun advantageously, with telescopes of large apertures and high magnifying powers. Philos Trans R Soc 90:255–283. https://doi.org/10.1098/rstl.1800.0014
2. Kirchhoff G (1860) Ueber das Verhältniss zwischen dem Emissionsvermögen und dem Absorptionsvermögen der Körper für Wärme und Licht. Ann Phys 185:275–301. https://doi.org/10.1002/andp.18601850205
3. Stefan J (1881) Ueber die Beziehung zwischen der Wärmestrahlung und der Temperatur (Sur la relation entre le rayonnement calorifique et la température); Sitzungs berichte d. K. Akademie d. Wissenschaften in Wien, p. 84. J Phys Theor Appl 10:317–319. https://doi.org/10.1051/jphystap:0188100100031700

4. Boltzmann L (1884) Ableitung des Stefan'schen Gesetzes, betreffend die Abhängigkeit der Wärmestrahlung von der Temperatur aus der electromagnetischen Lichttheorie. Ann Phys 258:291–294. https://doi.org/10.1002/andp.18842580616
5. Leopoldo N (1830) Description d'un thermo-multiplicateur ou thermoscope électrique. Bibliothèque Universelle des Sciences, Belles-Lettres et Arts 1830:225–234
6. Corsi C (2014) Infrared: a key Technology for Security Systems. In: Baldini F, D'Amico A, Di Natale C et al (eds) Sensors: proceedings of the first national conference on sensors, Rome 15–17 February, 2012, vol 162. Springer, New York, pp 37–42
7. Ishimwe R, Abutaleb K, Ahmed F (2014) Applications of thermal imaging in agriculture—a review. ARS 3:128–140. https://doi.org/10.4236/ars.2014.33011
8. Ring EFJ, Ammer K (2012) Infrared thermal imaging in medicine. Physiol Meas 33:R33–R46. https://doi.org/10.1088/0967-3334/33/3/R33
9. Lahiri BB, Bagavathiappan S, Jayakumar T et al (2012) Medical applications of infrared thermography: a review. Infrared Phys Technol 55:221–235. https://doi.org/10.1016/j.infrared.2012.03.007
10. McCafferty DJ (2013) Applications of thermal imaging in avian science. Ibis 155:4–15. https://doi.org/10.1111/ibi.12010
11. Taylor T, Counsell J, Gill S (2013) Energy efficiency is more than skin deep: improving construction quality control in new-build housing using thermography. Energ Buildings 66:222–231. https://doi.org/10.1016/j.enbuild.2013.07.051
12. Pleşu R, Teodoriu G, Țăranu G (2012) Infrared thermography applications for buildings investigation. Bull Polytech Inst Jassy Constr Archit Sect 62:157–168
13. Alfredo Osornio-Rios R, Antonino-Daviu JA, de Jesus Romero-Troncoso R (2019) Recent industrial applications of Infrared thermography: a review. IEEE Trans Industr Inform 15:615–625. https://doi.org/10.1109/TII.2018.2884738
14. Vavilov V, Burleigh D (2020) Infrared thermography and thermal nondestructive testing. Springer, Cham
15. Mailhé C, Godin A, Veillère A et al (2021) Applicability of Infrared thermography for the detection of phase transitions in metal alloys. Appl Sci 11:8885. https://doi.org/10.3390/app11198885
16. Bonilla LC, Forero JC, Perez H et al (2021) Prediction of refractory lining thickness in an electric furnace using thermography as a non-destructive testing technique. In: Rizzo P, Milazzo A (eds) European workshop on structural health monitoring: special collection of 2020 papers – volume 2, vol 128, 1st edn. Springer International Publishing, Springer, Cham, pp 289–298
17. Chakraborty B, Sinha BK (2020) Process-integrated steel ladle monitoring, based on infrared imaging – a robust approach to avoid ladle breakout. Quant InfraRed Thermogr J 17:169–191. https://doi.org/10.1080/17686733.2019.1639112
18. Bonilla LC, Forero JC, Perez H et al (2021) Assesment of thermography as a non-destructive testing technique to structural health monitoring of an electric furnace. In: Rizzo P, Milazzo A (eds) European workshop on structural health monitoring: special collection of 2020 papers – volume 2, 1st edn. Springer International Publishing, Cham, pp 299–308
19. Patra P, Sarkar A, Tiwari A (2019) Infrared-based slag monitoring and detection system based on computer vision for basic oxygen furnace. Ironmak Steelmak 46:692–697. https://doi.org/10.1080/03019233.2018.1460909
20. Pan D, Jiang Z, Chen Z et al (2018) Temperature measurement method for blast furnace molten iron based on infrared thermography and temperature reduction model. Sensors (Basel) 18:3792. https://doi.org/10.3390/s18113792
21. Minkina W (2009) Infrared thermography: errors and uncertainties. Wiley, Chichester/West Sussex/Hoboken
22. Sarawade AA, Charniya NN (2019) Infrared thermography and its applications: a review. In: 2018 3rd international conference on communication and electronics systems (ICCES) 2018, pp 280–285. https://doi.org/10.1109/CESYS.2018.8723875
23. Tsai P-F, Liao C-H, Yuan S-M (2022) Using deep learning with thermal imaging for human detection in heavy smoke scenarios. Sensors 22:5351. https://doi.org/10.3390/s22145351
24. Zhang Y, Li Q, Zhou H (2016) Theoretical foundation and basic properties of thermal radiation. In: Zhang Y, Li Q, Zhou H (eds) Theory and calculation of heat transfer in furnaces, 1. Aufl. Elsevier Reference Monographs, pp 1–43
25. DIAS Infrared GmbH (2020) PYROVIEW 768N: Hochauflösende Wärmebildkamera für Temperaturmessungen bis zu 3000 °C. https://www.dias-infrared.de/pdf/pyroview768n_ger_mail.pdf. Accessed 13 Feb 2023
26. Bale CW, Bélisle E, Chartrand P et al (2016) FactSage thermochemical software and databases, 2010–2016. Calphad 54:35–53. https://doi.org/10.1016/j.calphad.2016.05.002
27. DIN Deutsches Institut für Normung e. V. (2014) Thermoelemente_- Teil_1: Thermospannungen und Grenzabweichungen: Deutsche Fassung 17.200.20(DIN EN 60584-1:2014-07). https://www.beuth.de/de/norm/din-en-60584-1/206126963. Accessed 21 Feb 2023